

# Thermo-Oxidative Induced Damage in Polymer Composites: Microstructure Image-Based Multi-Scale Modeling and Experimental Validation

Rafid M. Hussein<sup>1</sup> · K. Chandrashekhara<sup>1</sup>

Received: 1 October 2017 / Accepted: 19 October 2017 / Published online: 7 November 2017  
© Springer Science+Business Media B.V. 2017

**Abstract** A multi-scale modeling approach is presented to simulate and validate thermo-oxidation shrinkage and cracking damage of a high temperature polymer composite. The multi-scale approach investigates coupled transient diffusion-reaction and static structural at macro- to micro-scale. The micro-scale shrinkage deformation and cracking damage are simulated and validated using 2D and 3D simulations. Localized shrinkage displacement boundary conditions for the micro-scale simulations are determined from the respective meso- and macro-scale simulations, conducted for a cross-ply laminate. The meso-scale geometrical domain and the micro-scale geometry and mesh are developed using the object oriented finite element (OOF). The macro-scale shrinkage and weight loss are measured using unidirectional coupons and used to build the macro-shrinkage model. The cross-ply coupons are used to validate the macro-shrinkage model by the shrinkage profiles acquired using scanning electron images at the cracked surface. The macro-shrinkage model deformation shows a discrepancy when the micro-scale image-based cracking is computed. The local maximum shrinkage strain is assumed to be 13 times the maximum macro-shrinkage strain of  $2.5 \times 10^{-5}$ , upon which the discrepancy is minimized. The microcrack damage of the composite is modeled using a static elastic analysis with extended finite element and cohesive surfaces by considering the modulus spatial evolution. The 3D shrinkage displacements are fed to the model using node-wise boundary/domain conditions of the respective oxidized region. Microcrack simulation results: length, meander, and opening are closely matched to the crack in the area of interest for the scanning electron images.

**Keywords** Thermo-oxidative damage · Object oriented finite element · Extended finite element · Traction-separation laws · High-temperature polymer matrix composites

---

✉ K. Chandrashekhara  
chandra@mst.edu

<sup>1</sup> Department of Mechanical and Aerospace Engineering, Missouri University of Science and Technology, Rolla, MO 65409, USA

## 1 Introduction

The investigation of mechanical behavior and damage of composites entails the analysis of fiber and matrix and their respective spatial distribution in the composite domain. The distribution of fibers in the matrix is either random or indeterminate. Micro-scale damage is localized and dependent on the microstructural characteristic. An isomorphic microstructure can be built to closely model the composite behavior using finite element analysis (FEA). The National Institute of Standards and Technology (NIST) developed an object oriented finite element analysis (OOF) tool to analyze materials' behavior using microstructural images [1–4]. In the field of polymer composites/nanocomposites, OOF was used to investigate mechanical properties, especially the elastic modulus.

Goel et al. [5] investigated the elastic modulus of a chopped glass fiber and polypropylene matrix thermoplastic composite. Optical images were acquired for polished samples and meshed using triangular elements with OOF. The fiber volume fraction was calculated from the images and used to estimate the modulus using analytical models. The analytical results showed a discrepancy from the experimental measurements. However, the predicted moduli using OOF were in a good agreement with the experimental findings. Dong and Bhattacharyya [6, 7] built a model to determine the tensile modulus of polypropylene/organoclay nanocomposites at various clay contents using OOF. Scanning/transmission electron microscopy was utilized to capture the microstructural images. Quadrilateral mesh was generated for the images acquired by scanning and transmission electron microscopy in OOF and used for FEA simulations. Experimental results of the modulus were compared to the FEA results and six analytical models using different aspect ratios. In all cases, OOF-based modulus results showed a close match to the experimental outcomes.

High temperature polymer matrix composites are susceptible to superficial thermal oxidation. During the propagation of oxidized layer, weight loss, density increase, and volumetric shrinkage take place. Due to volumetric shrinkage, strain and stress fields are built up, leading to matrix cracking [8]. Initiation and evolution of thermo-oxidation-induced cracking/damage at the micro-scale has not been investigated comprehensively in the literature. In the micro-scale, most of the previous investigations focused on the measurement/simulation of the shrinkage stresses/strains. Pochiraju et al. [9] presented a study on G30–500/PMR-15 unidirectional composites using representative volume elements (RVE) as a basis for diffusivity homogenization and oxidation shrinkage simulation. Simulation results determined that the peak stress due to lamina shrinkage after 200 h of oxidation was located at the fiber matrix interface. Localized shrinkage due to thermo-oxidation of IM7/977–2 carbon/epoxy unidirectional laminate was studied by Gigliotti et al. [10]. Viscoelastic polymer matrix behavior was coupled with a mechanistic diffusion-reaction scheme to model the local shrinkage of epoxy. Local shrinkage was measured using confocal interferometric spectroscopy and compared to the simulation. Results of shrinkage profiles indicated that volumetric shrinkage increased when the distance between fibers was increased.

Damage induced by thermo-oxidation was studied by a few investigators focusing on a homogenized composite domain. An and Pochiraju [11] simulated the oxidation and damage growth of bismaleimide (BMI) resin and cross-ply laminates. The analysis was implemented in the macro-scale for a neat resin plate subjected to bending and a laminated plate with a hole subjected to a tensile loading. The extended finite element method (XFEM) was used to simulate the crack propagation for the neat resin

case, while the Hashin-Rotem law was used for damage initiation of the laminate case. Liang and Pochiraju [12] presented a simulation scheme for the isothermal oxidation damage of unidirectional carbon polyimide composites. The shrinkage strain was assumed orthotropic and homogenized for the unidirectional laminate. Damage initiation was analyzed using Hashin's failure criteria. XFEM, cohesive elements, and a traction-separation law were used for modeling crack initiation and propagation. The cracking growth simulation results were compared to axial and transverse oxidation cracking measurements. The results matched closely for the aging time up to 1600 h. Daghia et al. [13] investigated the damage evolution in the transverse direction of oxidized superficial layers in thin cross-ply epoxy plates using a finite fracture mechanics approach. The damage kinetics was modeled in the meso-scale assuming a constant thickness of the oxidized layer to be half of the superficial ply thickness. A 2D FEA model was built to compute the strain energy change prior to and after cracking to be used for the calculation of the strain energy release rate. Cracks were artificially introduced, and the strain energy release rate was computed by considering thermal and oxidation shrinkage strains for soaking and cooling to room temperature.

In the current work, thermo-oxidation and oxidation shrinkage were investigated using a multi-scale approach. A 3D multi-scale simulations were conducted for macro-, meso- and, micro-scale. The macro- and meso-scale simulations were used to determine the local boundary conditions to simulate the shrinkage and damage in the micro-scale. Two micro-scale cases were investigated: a 2D case for oxidative shrinkage using an image-based mesh created by OOF, and a 3D case for oxidative cracking by extending the 2D image-based geometry of the first case to 3D. In the 2D case, the oxidative shrinkage was simulated and compared to the shrinkage in the scanning electron image. In the 3D case, the cracking damage was modeled using a mixed-mode model and XFEM approach. Aging experiments were conducted to measure weight loss and volumetric shrinkage using unidirectional bismaleimide laminates at 200°C up to 1000 h. Weight loss and volumetric shrinkage simulation results were then compared to the experimental findings. Another set of cross-ply laminate coupons were aged at 176°C and used to validate the macro-shrinkage model in the micro-scale using scanning electron images.

## 2 Modeling of Thermo-Oxidation

Modeling of the transient thermo-oxidation was implemented in the homogenized RVE level to determine the oxidized layer and weight loss. The micro-scale weight loss results were scaled by respective area ratios to the macro-scale as detailed below. This procedure can be used for any lay-up configuration; however, the RVE geometry should represent the microstructural aspects of the considered laminate. For a unidirectional laminate, the RVE geometry consisted of two fiber quarters centered at the rectangular matrix corners with dimensions  $3.14 \times 5.43 \times 135 \mu\text{m}$  with fiber volume fraction of 57.66%, as shown in Fig. 1. The x- and y-coordinate of the RVE represented transverse direction (perpendicular to fibers). By introducing homogenized properties of the RVE, Fick's second law of diffusion with a reaction term,  $R_{eff}(C, \varphi^{eff})$ , and a time-dependent oxidation state variable,  $\varphi^{eff}(t)$ , can be represented as the following equations:

$$\frac{\partial C(x, y, z, t)}{\partial t} = \bar{\nabla} \cdot \left( D_{eff}(\varphi^{eff}) \bar{\nabla} C(x, y, z, t) \right) - R_{eff}(C, \varphi^{eff}) \tag{1}$$

$$\frac{d\varphi^{eff}}{dt} = -\alpha(t, T)R_{eff}(C, \varphi^{eff}) \tag{2}$$

where  $C$  is the oxygen concentration;  $D_{eff}$  is the effective diffusivity; and  $\alpha(t, T)$  is a fitted proportionality parameter depending on time and temperature. The proportionality parameter was determined by fitting weight loss simulation results to the respective experimental outcomes throughout the oxidation time. Thermo-oxidation modeling proceeds in time and space domains following the three-zone model representation. Assuming that the fiber is unoxidized during thermo-oxidation, homogenization of the diffusivity and reaction term in Eqs. (1) and (2) can be obtained using the rule of mixtures [9]:

$$D_{eff}(\varphi^{eff}, T) = D_{eff}^{un}(T) \left\{ \frac{\varphi^{eff} - \varphi_{ox}^{eff}}{1 - \varphi_{ox}^{eff}} \right\} + D^{ox}(T) \left\{ \frac{1 - \varphi^{eff}}{1 - \varphi_{ox}^{eff}} \right\} \tag{3}$$

$$R_{eff}(C, \phi^{eff}, T) = R_0^{eff}(T) \left\{ \frac{\phi - \phi_{ox}^{eff}}{1 - \phi_{ox}^{eff}} \right\} \left[ \frac{2\beta C}{1 + \beta C} \left( 1 - \frac{\beta C}{2(1 + \beta C)} \right) \right] \tag{4}$$

$$R_0^{eff}(T) = V_m R_0^m(T) \tag{5}$$

$$\varphi_{ox}^{eff} = \varphi_{ox}^m(1 - V_f) + V_f \varphi_{ox}^f \tag{6}$$

where  $D_{eff}^{un}$  and  $D^{ox}$  are the unoxidized composite effective diffusivity and oxidized matrix diffusivity represented by Arrhenius forms, respectively. In the present simulation, the rule of mixtures was applied to the reaction rate constant,  $R_0^m(T)$ , and the oxidation state variable,  $\varphi_{ox}^m$  of matrix. As the fiber was assumed unoxidized,  $\varphi_{ox}^f$  was set equal to unity. In isothermal oxidation, temperature is constant in Eqs. (3) and (5).

The RVE orthotropic effective diffusivity can be estimated using the averaging method by solving a steady-state simulation for a unit volume RVE. The steady-state concentration field,  $C(x, y, z)$ , and the diffusivity tensor of the matrix and fiber,  $D(x, y, z)$ , were used to estimate the effective diffusivity by the volume averaging method [14]:

$$D_{eff}(i) = \int_0^a \int_0^b \int_0^c D_{iq}(x_1, x_2, x_3) \frac{\partial C(x_1, x_2, x_3)}{\partial x_i} dx_1 dx_2 dx_3 \quad i, q = 1, 2, 3 \tag{7}$$

where  $D_{eff}$  is the homogenized diffusivity;  $D_{iq}$  is the diffusivity tensor of fiber and matrix;  $a, b$ , and  $c$  are the geometrical limits of the scaled RVE; and  $x_1, x_2, x_3$  are  $x, y, z$ .

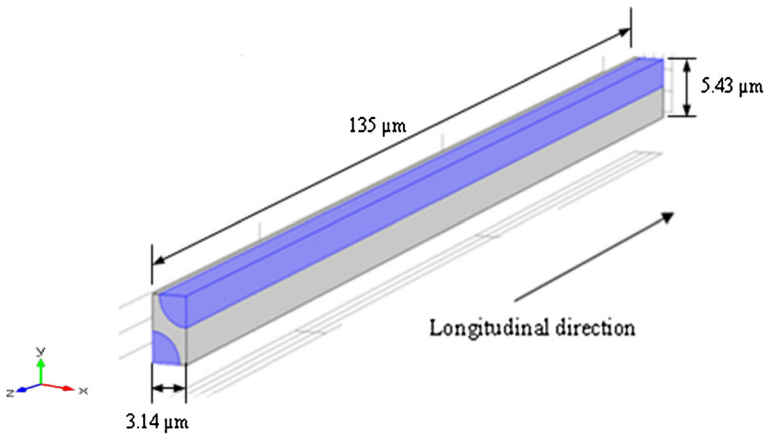


**Fig. 1** RVE geometry of a unidirectional lay-up (fibers are highlighted)

Henry’s law for sorption was used to calculate oxygen concentration at the boundaries:

$$C|_b = S \times P \tag{8}$$

Solubility,  $S$ , is a temperature-independent parameter where  $S = 3.61 \times 10^{-4} \text{ mol/m}^3\text{Pa}$  for BMI. Oxygen partial pressure,  $P$ , is calculated as 0.21 of the air pressure at the aging temperature.

The following integral was introduced for weight loss due to oxidation by considering an infinitesimal homogenized element of volume  $dv = dx dy dz$  undergoing thermal oxidation:

$$W_{loss}(t) = \rho_0 \iiint_{matrix} (I-\varphi)dv \tag{9}$$

where  $\rho_0$  is the density of the unoxidized polymer matrix calculated from the unoxidized composite density ( $\rho_c$ ). A scaling procedure was introduced by the respective surface area ratio of the sample to RVE. In all cases, the sample’s surface area was calculated from initial measurements in the longitudinal and transverse simulations:

$$W_{loss} = W_{loss}^r(x) \times \frac{A_x^s}{A_x^r} + W_{loss}^r(y) \times \frac{A_y^s}{A_y^r} + W_{loss}^r(z) \times \frac{A_z^s}{A_z^r} \tag{10}$$

where  $W_{loss}$  is the total weight loss in the sample’s scale;  $W_{loss}^r(x)$ ,  $W_{loss}^r(y)$ , and  $W_{loss}^r(z)$  are the weight loss per RVE due to oxidation in  $x, y$ , and  $z$  calculated using the volume integral of Eq. (9); and  $A_x^s$  and  $A_x^r$  are the areas of oxidation-exposed surface perpendicular to  $x$ -direction in the sample and the RVE, respectively. Similarly,  $A_y^s, A_z^s$  and  $A_y^r, A_z^r$  are the exposed surface areas in their respective scales and directions. The surface area ratio of the sample to the RVE was considered equivalent to a unique number that defines the number of RVEs in a surface area. Then,  $A_x^s/A_x^r$  was equivalent to the number of RVEs in the oxidation-exposed surfaces perpendicular to  $x$ -direction. A similar definition was introduced for  $A_y^s/A_y^r$  and  $A_z^s/A_z^r$  in their respective directions. The number of RVEs was constant based on the initial sample’s area, even though matrix shrinkage had taken place throughout the oxidation process. The presence of cracks due to matrix shrinkage and residual stresses had an effect on the area ratios; however, the crack surface area was hard to measure or calculate precisely. Fitting the simulation results

to experimental results by introducing  $\alpha(t, T)$  can handle the effect of the growing crack in the surface area. Time and temperature dependence of  $\alpha(t, T)$  were assumed isotropic in longitudinal and transverse thermo-oxidation. All simulations in this section were implemented in COMSOL Multiphysics using the properties listed in Table 1.

### 3 Modeling Volumetric Shrinkage Strains

Shrinkage of matrix during thermo-oxidation produces strains in the composite, which varies linearly with  $\varphi^{eff}(t)$  [15]:

$$\varepsilon_s(\phi^{eff}) = \varepsilon_s^{ox} \times \left( \frac{1 - \phi^{eff}}{1 - \phi_{ox}^{eff}} \right) \tag{11}$$

where  $\varepsilon_s$  is the linear shrinkage strain of the matrix due to oxidation. For a completely oxidized matrix, shrinkage strain attains its maximum value of  $\varepsilon_s^{ox}$ . The shrinkage strain of Eq. (11) is isotropic and depends only on  $\varphi^{eff}(t)$ . Volumetric shrinkage measurements of unidirectional samples was used to determine  $\varepsilon_s^{ox}$  by fitting simulation results to the experimental outcomes. It should be noted that the maximum shrinkage strain is a matrix property, which is lay-up and temperature-independent in the service temperature range of BMIs.

The volumetric shrinkage was modeled in the RVE micro-scale for the three principal directions of x, y, and z corresponding to transverse-x and -y and longitudinal-z. The volumetric shrinkage in the sample macro-scale,  $S_V$ , was determined using:

$$S_V = \frac{\Delta V}{V} \tag{12}$$

where  $\Delta V$  is the total change in volume due to oxidation shrinkage for a sample of initial volume  $V$ , as shown in Fig. 2. It should be noted that the notation of Eq. (10) was used in this figure. The later definition of volumetric shrinkage can be expanded as follows:

**Table 1** Parameters used in thermo-oxidation simulation of a unidirectional laminate

Parameter	Symbol	Value
Diffusivity of the unoxidized matrix ( $\varphi=1$ )	$D_0^{un}$	$1.62 \times 10^{-4}$ mm <sup>2</sup> /min
Diffusivity of the oxidized matrix ( $\varphi=\varphi_{ox}$ )	$D_0^{ox}$	$1.94 \times 10^{-4}$ mm <sup>2</sup> /min
Longitudinal fiber diffusivity	$D_L^f$	$D_0^{un}/10^3$
Transverse fiber diffusivity	$D_T^f$	$D_0^{un}/10^5$
Density of laminate <sup>a</sup>	$\rho_c$	1.57 g/cm <sup>3</sup>
Density of unoxidized polymer matrix <sup>c</sup>	$\rho_o$	1.24 g/cm <sup>3</sup>
Fiber weight fraction <sup>b</sup>	$W_f$	65.3%
Density of fiber	$\rho_f$	1.78 g/cm <sup>3</sup>
Fiber volume fraction <sup>c</sup>	$V_f$	57.66%
Homogenized transverse-x diffusivity	$D_X^{eff}$	$5.69 \times 10^{-5}$ mm <sup>2</sup> /min
Homogenized transverse-y diffusivity	$D_Y^{eff}$	$3.29 \times 10^{-5}$ mm <sup>2</sup> /min
Homogenized longitudinal-z diffusivity	$D_Z^{eff}$	$6.86 \times 10^{-4}$ mm <sup>2</sup> /min

<sup>a</sup> determined experimentally by water displacement according to ASTM D792

<sup>b</sup> manufacturer’s data sheet

<sup>c</sup> determined using calculation methods of ASTM D3171

$$S_V = \frac{\Delta V}{V} = \frac{\Delta V_{Tx}}{V} + \frac{\Delta V_{Ty}}{V} + \frac{\Delta V_{Lz}}{V}$$

where  $\Delta V_{Tx}$ ,  $\Delta V_{Ty}$ , and  $\Delta V_{Lz}$  are the components of volume change in  $x$ ,  $y$ , and  $z$ . Reformulating the last equation by introducing the number of RVEs in a principal direction results in:

$$\frac{\Delta V_{Tx}}{V} = \frac{\Delta V_{RVEx} \times N_{RVEx}}{V_{RVEx} \times N_{RVEx}}$$

where  $\Delta V_{RVEx}$  is the change in RVE volume due to oxidation in the  $x$ -direction and  $N_{RVEx}$  is the number of RVEs in the respective  $x$ -direction. Similar definitions for the change in volume and number of RVEs were used for the  $y$ - and  $z$ -directions. Substituting the last definitions of all principal directions in Eq. (12) yields the total volumetric shrinkage in the sample scale:

$$S_V = \frac{\Delta V_{RVEx}}{V_{RVEx}} + \frac{\Delta V_{RVEy}}{V_{RVEy}} + \frac{\Delta V_{RVEz}}{V_{RVEz}} \tag{13}$$

Elastic properties of the composite laminate for the oxidative shrinkage simulations are listed in Table 2. The simulation results were compared to the experimental measurements of the samples' shrinkage to determine the maximum oxidative shrinkage strain,  $\epsilon_s^{\text{ox}}$ . This parameter was later used in the multi-scale modeling of the next part.

### 4 Multi-Scale Modeling of Shrinkage Damage

The analysis of this section was performed to investigate the volumetric shrinkage and cracking damage of the surface layer of a cross-ply laminate aged under 176°C for 1000 h. The homogenized diffusivities and proportionality parameter  $\alpha(t, T)$  for the cross-ply laminate were determined elsewhere [18] and are listed in Table 3.

The important step in modeling a multi-scale domain is determining the boundary conditions for the meso- and micro-scale subdomains from the macro-scale domain. The modeling procedure of the current work was a 3D macro-scale simulation in the sample level, a 3D

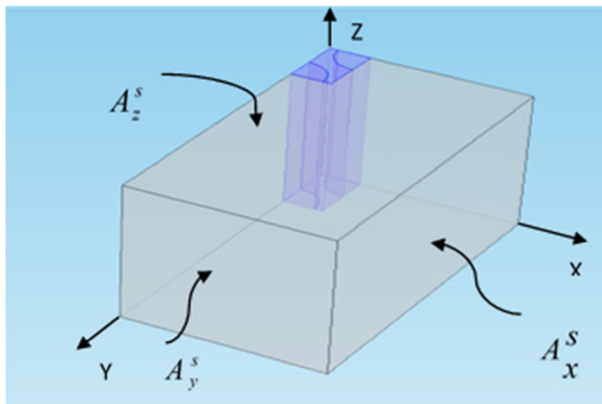


**Fig. 2** Schematic of a unidirectional sample with initial volume  $V$  (RVE is highlighted)

**Table 2** Elastic constants of the homogenized RVE

Property	Symbol	Value
Longitudinal tensile modulus <sup>a</sup>	$E_{zz}$	$142.03 \times 10^9$ Pa
Transverse tensile modulus <sup>a</sup>	$E_{xx}, E_{yy}$	$11.03 \times 10^9$ Pa
Longitudinal Poisson’s ratio <sup>b</sup>	$\nu_{xy}$	0.4
Transverse Poisson’s ratio <sup>a</sup>	$\nu_{zy}, \nu_{zx}$	0.29
Longitudinal shear modulus <sup>c</sup>	$G_{xy}$	$16.11 \times 10^9$ Pa
Transverse shear modulus <sup>a</sup>	$G_{zx}, G_{zy}$	$24.82 \times 10^9$ Pa

<sup>a</sup> manufacturer’s data sheet

<sup>b</sup> Haque et al. [16]

<sup>c</sup> determined using calculation methods of compliance terms [17]

meso-scale simulation followed by two micro-scale simulations in 2D and 3D domains. Transient thermo-oxidation and static structural problems were solved at all scales by introducing the shrinkage strains of the previous section.

### 4.1 Macro-Scale Modeling

The geometrical domain of this simulation was equivalent to the real SEM sample in length dimension of 1 in. (0.0254 m). However, the depth was reduced to 1 mm to save computational time as shown in Fig. 3. Due to symmetry, the macro-scale geometry was built using only the top 8 layers with smeared properties. For thermo-oxidation, the oxygen concentration boundary condition of  $C_b = 7.678 \text{ mol/m}^3$  was assigned to the faces pointed to by dashed arrows in the figure.

It should be noted that the front face of the laminate was not assigned a concentration boundary condition (oxidation-free) because samples were cut periodically for 1000 h, rendering the front face intact by oxidation. The top surface of the top layer, pointed to by the dashed arrow, was assigned a displacement constraint in the x- and z-direction, allowing shrinkage displacement in the y-direction only. Due to symmetry, the bottom surface of the domain was constrained in the y-direction only by assigning a zero y-displacement.

### 4.2 Meso-Scale Modeling

The meso-scale domain is shown in Fig. 4 with the top layer highlighted and enlarged to show fibers and matrix. The length and width were  $1 \times 10^{-4}$  m for the x-z cross-section. The depth composed of 8 layers, as was the macro-scale domain. Thermo-oxidation simulation was conducted by assigning an oxygen boundary condition of  $C_b$  for the top face of the first layer, as pointed to by a dashed arrow in Fig. 4.

**Table 3** Homogenized cross-ply diffusion-reaction parameters

Parameter	Symbol	Value
Homogenized transverse-x diffusivity <sup>a</sup>	$D_x^{eff}$	$11.9 \times 10^{-4} \text{ mm}^2/\text{min}$
Homogenized transverse-y diffusivity	$D_y^{eff}$	$62.7 \times 10^{-4} \text{ mm}^2/\text{min}$
Homogenized longitudinal-z diffusivity	$D_z^{eff}$	$62.7 \times 10^{-4} \text{ mm}^2/\text{min}$
Proportionality parameter	$\alpha(t, T)$	$\begin{cases} 25 \times 10^{-5}, & t \leq 200hr, t > 200hr. \\ 1.8 \times 10^{-5} e^{(6.75 \times 10^{-7} \times t)}, & t > 200hr. \end{cases}$

<sup>a</sup> through-thickness diffusivity



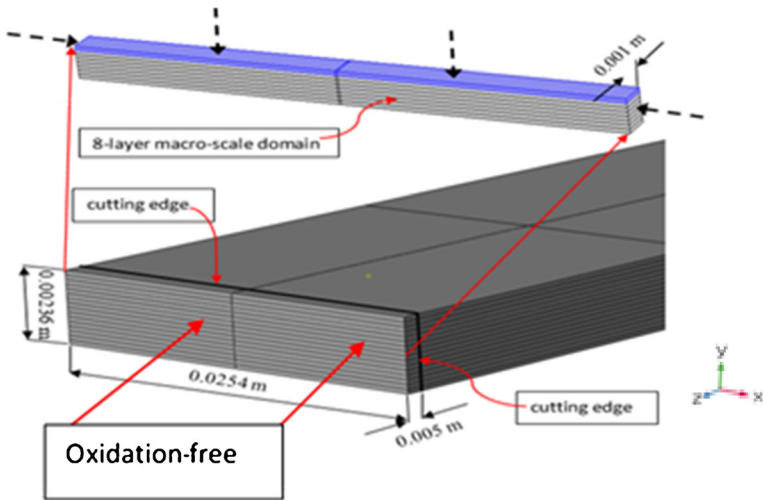


**Fig. 3** Eight-layer macro-scale domain (top layer is highlighted)

Fiber locations in the first layer were determined from the coordinates of the OOF mesh, shown in the next section, and extruded through the depth to generate 3D fiber and matrix domains. Extra fibers were added by duplication of the original fibers to the left, right, and bottom of the OOF mesh fibers to consider the effect of adjacent fibers on the micro-scale case. The left and right faces perpendicular to the x-direction, layers 2–8 from top to bottom, were assigned displacement boundary conditions in three principal directions. These boundary conditions were taken from the results of the macro-scale simulation and assigned to the respective faces. The bottom surface of layer 8 was constrained by assigning a zero displacement in the y-direction as in the macro-scale case.

### 4.3 Micro-Scale Modeling

The micro-scale models simulated 2D oxidative shrinkage and 3D cracking damage. The 2D case used an OOF-generated mesh to solve for the oxidative shrinkage. The 3D case utilized

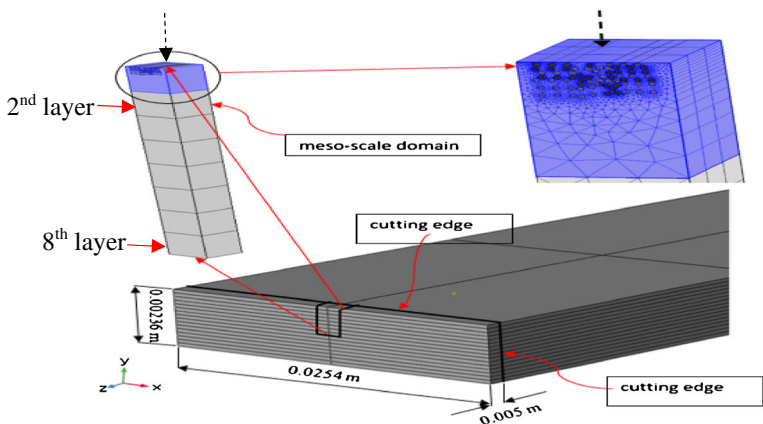


**Fig. 4** Meso-scale domain (top layer matrix is highlighted)

the geometrical distribution of fibers in the OOF mesh to build the 3D geometry for crack simulation.

#### 4.3.1 2D Micro-Scale

A 2D transient thermo-oxidation was run to determine the oxidation distribution using a quad-based mesh generated for a scanning electron micrograph of a superficial layer in a cross-ply laminate. The laminate was aged for 500 h under the conditions described in the experimental part of this work. The simulation aimed to analyze the local shrinkage due to oxidative strain. The mesh was created using OOF by pixel discretizing of the image shown in Fig. 5.

This mesh was generated using 80 quad elements for the  $x$ - and  $y$ -direction of the mesh skeleton. The skeleton elements of the fiber/matrix interface region was refined once using a default refinement to ensure a good mesh representation of the interface region. The final mesh consisted of about 25,000 quad elements grouped by a 36-fiber and matrix domain. The mesh was imported to Nastran and the element type was converted to CQUAD4, which is a 4-node plain strain element that is compatible with Comsol.

The oxidation evolution over 1000 h was simulated using a two-coefficient form partial differential model for fiber and matrix domains. The oxygen boundary condition of  $C_b$  was imposed on the top line of the mesh only where oxidation evolves in  $y$ -direction. The oxidized layer shrinkage followed the linear strain that was introduced as the input for a static elastic model. The displacement boundary conditions for the elastic structural model were taken from the meso-scale model and imposed as a linear-spline function generated using Comsol. These boundary conditions were imposed on the left, right, and bottom lines of the mesh.

#### 4.3.2 3D Micro-Scale

Oxidation-induced cracking was modeled in a 3D domain to account for a mixed-mode cracking where the displacement in the  $z$ -direction was considered as shown in Fig. 6. Orange arrows represent the oxidized layer nodes of the matrix (colored by green), blue arrows represent fiber constraints. The 3D domain was created in Abaqus using the geometrical distribution of fibers in the OOF mesh. The 3D micro-domain was created in the mid-distance of depth ( $z$ -

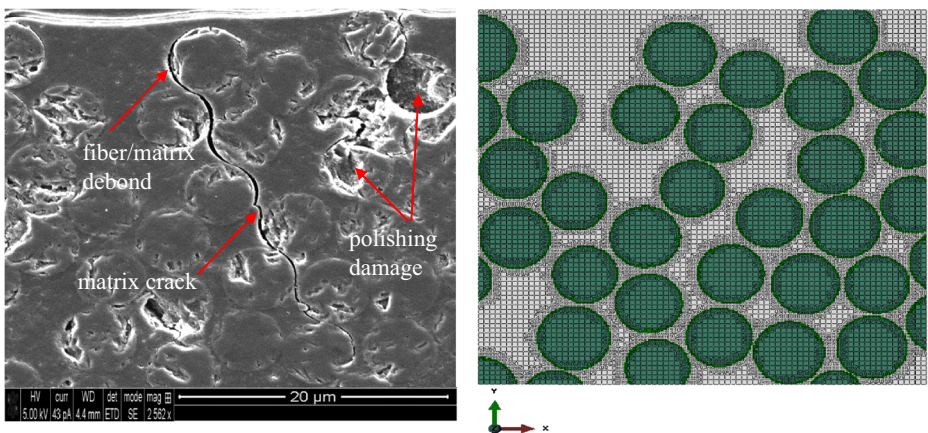


**Fig. 5** The scanning electron micrograph and the respective OOF mesh

direction) of the first layer in the meso-scale domain. The dimensions of the micro-domain were  $33.75 \mu\text{m} \times 32 \mu\text{m} \times 0.5 \mu\text{m}$ . Due to the limitations of a small geometric representation in Abaqus, the unit length was set to  $1 \mu\text{m}$ , and all material properties were scaled accordingly. The boundary conditions were imported from Comsol in the input file per node by creating sets for completely oxidized nodes. A total of 2886 sets were created and assigned displacement boundary conditions in a 3D frame for the matrix nodes only (marked by orange arrows). Only fiber nodes of the front surfaces were constrained by assigning zero displacement in the z-direction. As fibers are unoxidized and have a larger modulus compared to matrix, the fiber faces' constraint was warranted.

In the present work, the crack initiation and propagation were modeled using the XFEM under the traction-separation cohesive behavior. The crack interaction was defined using a separate set to include the enrichment degrees of freedom for the XFEM crack, as shown in Fig. 7a. No constraints were imposed on the crack path, which was arbitrary and solution-dependent in the defined set. The crack interaction set was also created to localize cracking damage and take into consideration the strength and toughness variability throughout the composite. Mechanical properties of a composite vary from point to point due to microstructural heterogeneity [19]. Lamina strength variation is dependent on fiber spacing, void distribution, and microstructural changes due to oxidation [20]. However, mechanical properties of all elements inside all sets were assumed constant.

In the XFEM, the finite element approximation is enriched with discontinuous terms to account for the crack tip and crack surface singularities. For a 1D standard XFEM approximation [21]:

$$u(x) = \sum_{j=1}^n u_j \psi_j(x) + \sum_{j=1}^m a_j \psi_j^*(x) H_j(x) \quad (14)$$

where  $u_j$ ,  $\psi_j(x)$  and  $H_j(x)$  are the nodal displacement, normal shape function and the enrichment function. The function  $\psi_j^*(x)$  is also a normal shape function that can be equal to  $\psi_j(x)$ . The enriched degree of freedom,  $a_j$  is defined for each node in the enriched domain of nodes  $m$ .

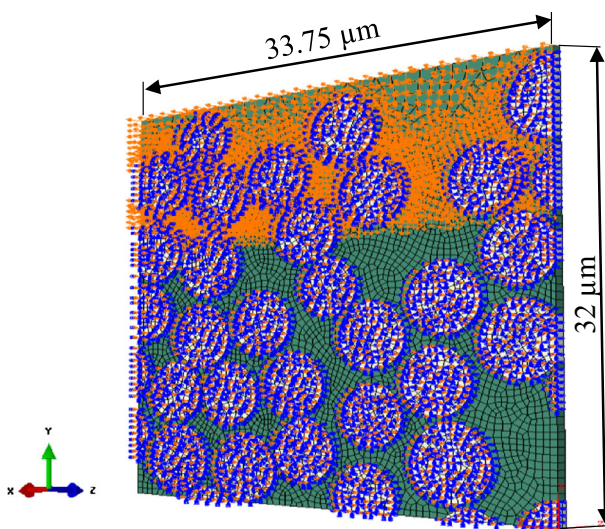


**Fig. 6** 3D damage model and boundary conditions

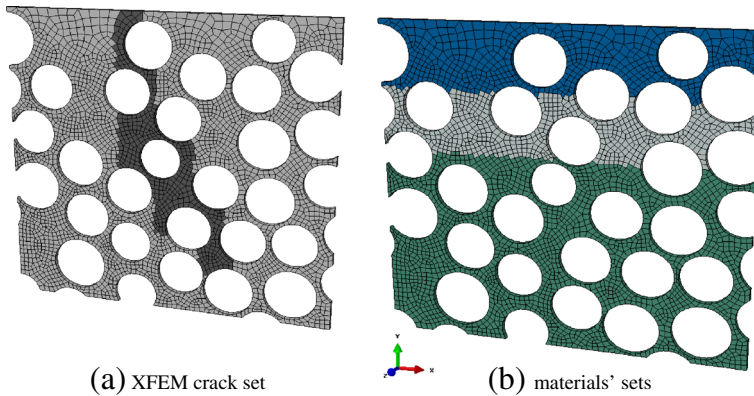


**Fig. 7** Matrix materials' and XFEM crack sets

Details of the XFEM derivation and implementation for the fracture and delamination in composites are out of the scope of the current work and can be found in [22, 23].

The fiber/matrix interface was defined as a cohesive surface transmitting the shrinkage displacements to the fibers. The evolution of the oxidized layer was accompanied by a change in elastic properties that was proportional to the oxidation state. The modulus evolution after 1000 h of aging was accounted for by defining three materials' sets in Abaqus. These materials' sets represented the completely oxidized (blue-colored), active oxidation (gray-colored), and intact matrix (green-colored) materials marked by colored elements from top to bottom, as shown in Fig. 7b. The modulus evolution was assumed linearly-dependent on the oxidation state for the range  $4.6 \text{ GPa} \leq E(\varphi) \leq 5.2 \text{ GPa}$  [11].

A maximum principal stress criterion was adopted to determine the failure initiation of the matrix and cohesive interfaces. The damage evolution was modeled using a bilinear traction-separation law with a mixed mode behavior, as shown in Fig. 8. Oxidation shrinkage induces stresses elastically until the critical maximum principal stress,  $S_{\max}$ , is reached where cracking damage starts and evolves up to the maximum separation,  $\delta_{\max}$ , which is determined by the fracture energy,  $G(\delta)$ . A fracture energy-based Benzeggagh–Kenane (BK) criterion was selected for the mixed-mode cracking behavior with the power parameter set to unity. Due to the mixed-mode fracture, normal and shear mode energies were assumed constant and independent of the oxidation state. The cohesive surfaces between the fibers and matrix were assigned stiffness constants of unity. The damage initiation maximum stresses and fracture energies of the matrix, cohesive surfaces are listed in Table 4.

## 5 Experimental Procedure

Unidirectional test specimens measuring  $3 \times 3$  in. ( $76.2 \times 76.2$  mm) were cut from a unidirectional laminate using a low speed saw. Samples were dried in a convection oven at  $70^\circ\text{C}$  for 20 h. Initial weights and dimensions were measured, and samples were placed in the oven for aging at  $200^\circ\text{C}$ . Test samples were removed at regular intervals so that the weight loss and volumetric shrinkage could be recorded. A pressure vessel was required to conduct aging studies in argon. A cylindrical steel vessel, 50 cm long with an inside diameter of 10 cm, was used (Fig. 9). Samples were placed inside the pressure vessel, which was then filled with argon at  $38.32 \pm 3$  kPa at room temperature. The pressure inside the vessel was about 101.32 kPa at  $176^\circ\text{C}$ .

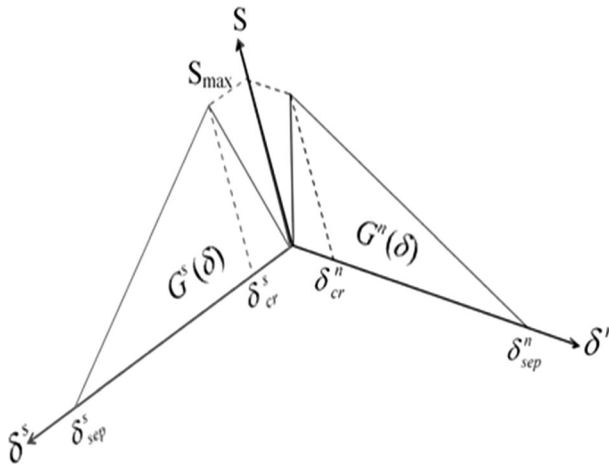


**Fig. 8** Traction-separation law for damage evolution

Seven samples were used to obtain weight loss measurements, four in air and three in argon. Two samples were used for measuring volumetric shrinkage in both cases. Samples were allowed to cool down for 15 min inside the oven and moved to a desiccator. Samples were then allowed to cool down to room temperature under vacuum. As recommended by ASTM D2126, fifteen measurements were taken per sample using a micrometer to calculate volumetric shrinkage. Sample mass was measured using a high precision balance with a least count of 0.1 mg.

Two coupons of a cross-ply laminate measuring  $6 \times 1$  in. ( $152.4 \times 25.4$  mm) were also aged under similar conditions. These were used to cut the scanning electron microscopy (SEM) samples upon removal of the coupons from the oven. SEM samples were embedded in epoxy and polished progressively. The SEM images were acquired by a dual-beam Helios 600 electron microscope using an accelerating voltage of 5 kV and a beam current of 43 pA. The working distance was in the range of 3.4 to 4.4 mm.

## 6 Results and Discussion

### 6.1 Thermo-Oxidation Modelling and Experiments

Results of thermo-oxidative aging are shown in Fig. 10a. The weight loss of samples in air was higher than the weight loss in argon for all aging hours. The average weight loss ratio was 0.72 and 0.12% at 1000 h for air-aged and argon-aged coupons. The weight loss of both cases was

**Table 4** Damage initiation and propagation properties

Property	Symbol	Value
Maximum principal stress (unoxidized matrix)	$S_{max}$	$1.6 \times 10^{-5}$ Pa
Maximum principal stress (oxidized/active oxidation matrix)	$S'_{max}$	$1.6 \times 10^{-5}$ Pa
Maximum nominal stress (cohesive surfaces)	$S_n$	$S_{max}/1000$
Fracture energy	$G$	$1 \times 10^{-5}$ J/m <sup>2</sup>
Viscosity stabilization coefficient	$\nu_s$	$1 \times 10^{-4}$



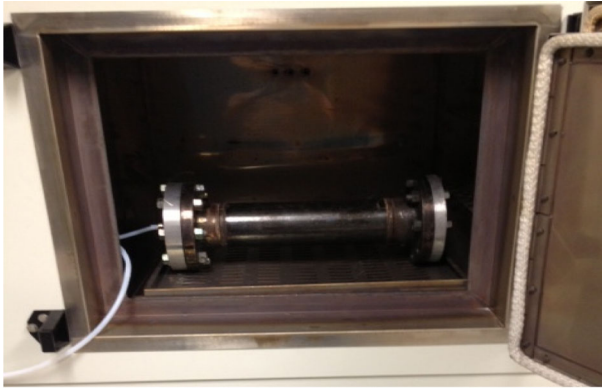


**Fig. 9** Chamber setup used for argon aging

linearly-dependent on aging time with a constant rate. These results indicate that the major cause of weight loss is an oxidation reaction. The contribution of polymer decomposition to weight loss in argon was insignificant.

A comparison of the weight loss simulation results and experimental findings are shown in Fig. 10b. The depicted results in the figure represent the total weight loss by incorporating the average percent contribution of polymer decomposition weight loss. Since the weight loss rate was approximately constant for the aging hours of this work, it was assumed that the proportionality parameter is one equation. Details of the weight loss simulation and scaling can be found in the author’s previous work [24]. The proportionality parameter was estimated by fitting simulation and experimental weight loss:

$$\alpha(t) = 4.5 \times 10^{-5} e^{(7.5 \times 10^{-7} \times t)} \tag{15}$$

where  $t$  is the aging time in seconds.

Volumetric shrinkage was measured using the volume difference between aged and unaged samples. The average volumetric shrinkage of two samples was taken as the final result. Measurements were started at 500 h when relatively measurable shrinkage was expected, as shown in Fig. 11a. The contribution of oxidation in weight loss and volumetric shrinkage is the difference between air-aged and argon-aged outcomes. The contribution of oxidation in weight loss was much higher than its contribution in volumetric shrinkage where polymer

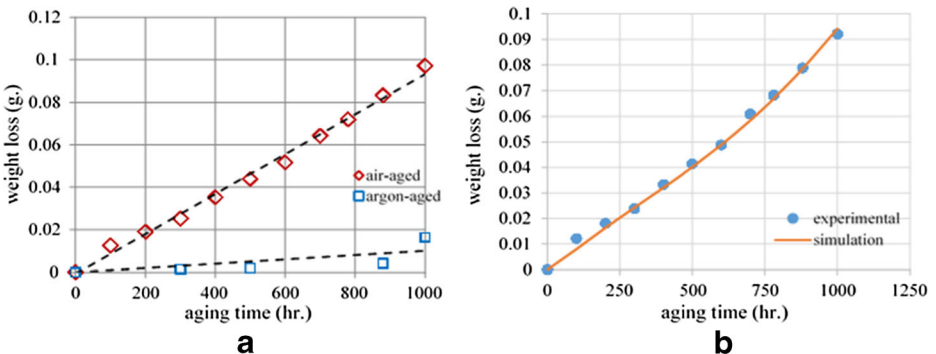


**Fig. 10** Weight loss results **a** experimental and **b** comparison with simulation

decomposition contributed significantly in the later. However, oxidative shrinkage was more significant in producing micro-cracks due to the constraint of the un-oxidized region. Polymer decomposition shrinkage was insignificant in producing micro-cracking damage as it happened through the whole polymer volume. In Fig. 11b, the maximum oxidative macro-shrinkage strain was determined by fitting the simulation and experimental results:

$$\varepsilon_s^{\alpha x} = 2.5 \times 10^{-5} \quad (16)$$

The simulation results are closely fitted to the experimental measurements using the proposed maximum shrinkage strain. Similar to the weight loss behavior, the shrinkage behavior followed a constant rate for linear dependence on aging time.

## 6.2 Multi-Scale Modeling Results

All simulations in this section were run at 176°C up to 1000 h to validate the oxidation shrinkage and cracking damage using 16-layer cross-ply numerical samples.

### 6.2.1 Macro-Scale and Meso-Scale Simulations

The oxidation state and shrinkage displacement fields of the macro-scale are shown in Fig. 12 for half of the domain, due to symmetry. The meso-domain is enlarged to show dimensions and location. The 3D displacement boundary conditions of the left and right faces of the meso-scale domain were extracted from the macro-scale results and converted to 2D linear interpolation functions. Layers 1–8 from top to bottom are shown in Fig. 12a. The displacement spike at the corner of the domain resulted from the numerical interaction between shrinkage in the z- and x-directions. However, the effect of the spike was minimal on the extracted boundary displacements. As mentioned in the modeling section, the interpolated boundary conditions will be applied to the right and left faces of layers 2–8 for the meso-scale simulation.

In Fig. 13, the oxidation state and shrinkage displacement evolution for the meso-scale simulation are shown. The first layer was enlarged to show the displacement and oxidation fields of the micro-domain. The 3D displacement boundary conditions for the micro-scale model were extracted from the results of the meso-scale simulation. The displacement boundary conditions were extracted for the front face of the micro-domain; front face is

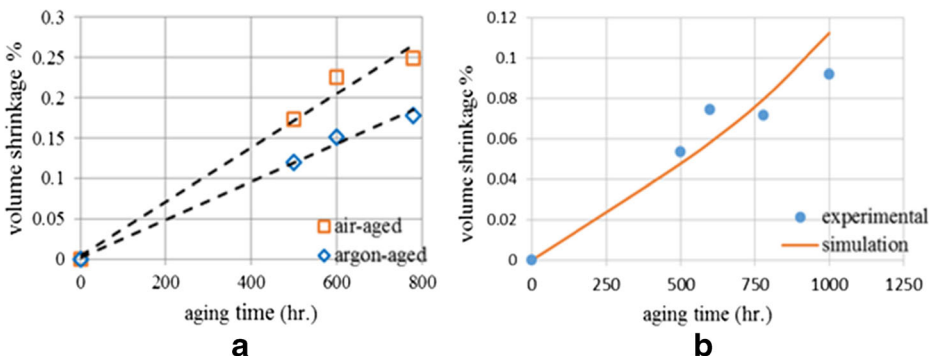


**Fig. 11** Volumetric shrinkage results **a** experimental and **b** comparison with simulation

perpendicular to the  $y$ -direction, as shown in Fig. 13b. The effect of fiber distribution on the shrinkage displacement is significant. The maximum shrinkage was located at the resin-rich region of the oxidized superficial layer. These boundary conditions were then applied to the 3D and 2D micro-scale simulations to investigate the shrinkage deformation and cracking, respectively.

6.2.2 Micro-Scale Simulation (2D)

The oxidation state, displacements in the  $x$ - and  $y$ -directions ( $u$  and  $v$ ), and the second principal stress ( $\sigma_{22}$ ) distribution for 500 h of aging are shown in Fig. 14. The results of this part were based on a local maximum shrinkage strain, as will be discussed later. In Fig. 14a, the oxidation state evolution is plotted for the composite domain. The completely oxidized layer

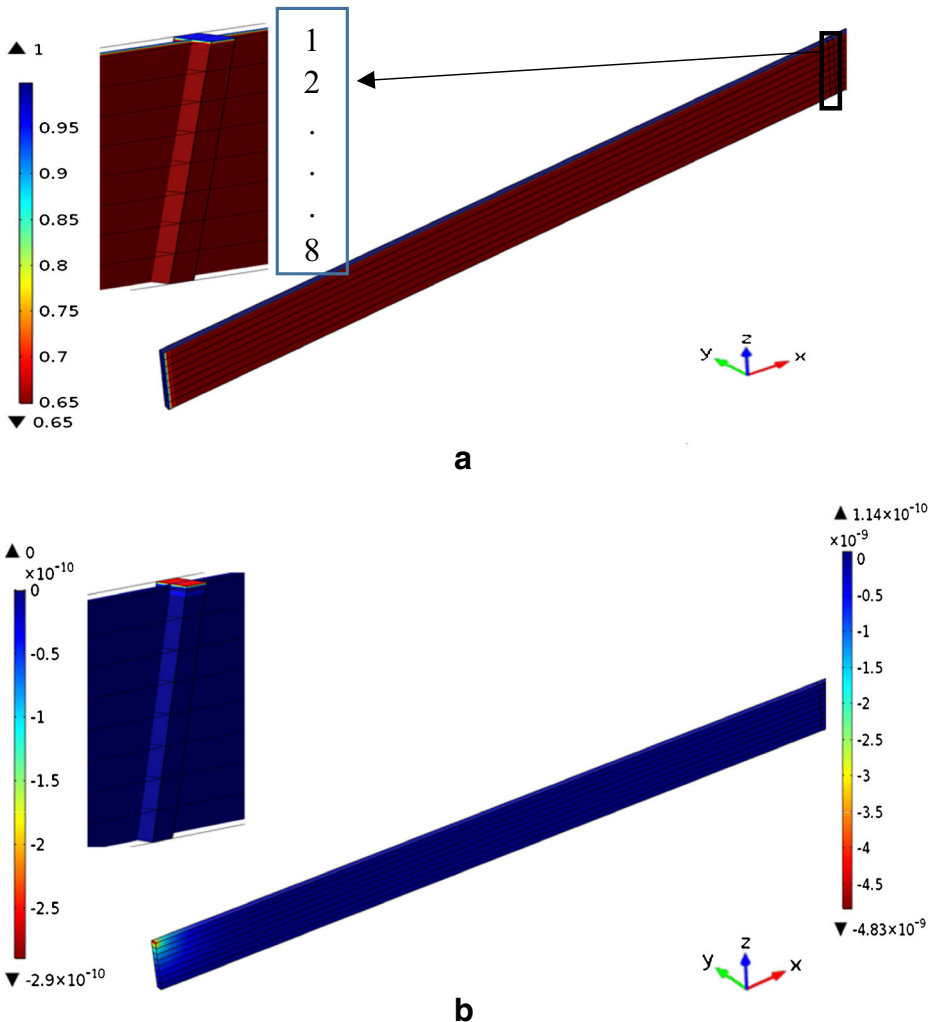
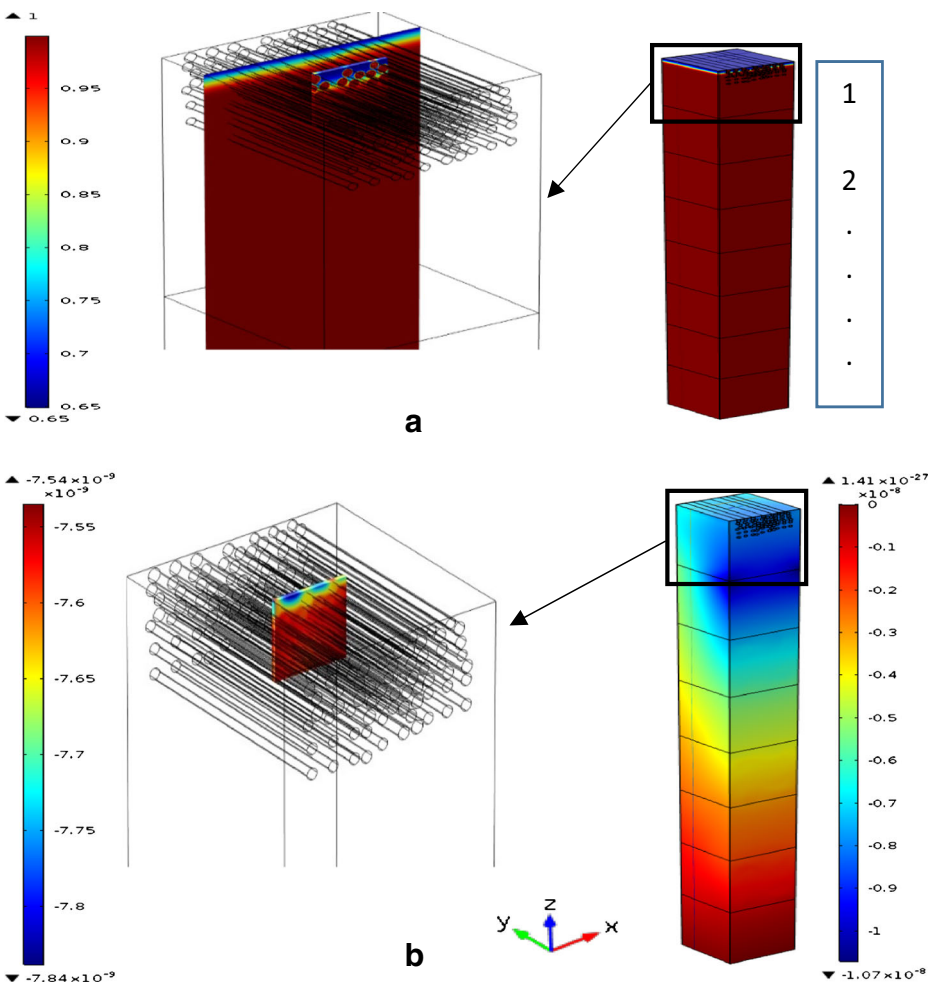


Fig. 12 Macro-scale results a oxidation state and b z-shrinkage displacement (w)



evolved for a couple of microns, leading to the shrinkage of the exposed surface. The average oxidized layer thickness was about 7.5  $\mu\text{m}$ . The oxidation shrinkage displacements are shown in Fig. 14b and c. The area of interest is marked by the arrow, where the region was under compression due to  $u$  displacement and downward stretch due to  $v$  displacement. The combined effect of the shrinkage displacements produced a compressive second principal stress ( $\sigma_{22}$ ), as shown in Fig. 14d. However, there were tensile stresses located at the fiber/matrix interfaces where the failure was expected to start. The concentration of stresses also favors the failure to start at the inner interfaces instead of the oxidation-exposed edge/surface. The magnitude of the tensile/compressive stresses were dependent on the elastic properties difference between fiber and matrix and the evolved shrinkage strain. It should be noted that the fiber volume fraction was also calculated for the simulated domains which yielded a value close to the globally calculated fiber volume fraction.

The global maximum shrinkage strain  $\epsilon_s^{ox} = 2.5 \times 10^{-5}$  was used first to simulate the shrinkage deformations and stresses. Simultaneously, cracking damage simulations were run,



**Fig. 13** Meso-scale results **a** oxidation state and **b** z-shrinkage displacement ( $w$ )

which showed that the global shrinkage strain was smaller to produce a crack of around  $30\ \mu\text{m}$  during the first 500 h of aging. Since the maximum shrinkage strain was a matrix property and due to the heterogeneity in matrix properties discussed earlier, it was assumed that the maximum shrinkage strain had a local variation. When the maximum shrinkage strain was scaled up by 13 to  $\varepsilon_s^{\text{ox}}(\text{local}) = 3.25 \times 10^{-4}$ , the cracking meander and length matched closely. Accordingly, this local value was used to produce the results in Fig. 14.

### 6.2.3 Micro-Scale Simulation (3D)

The oxidative micro-cracking or “spontaneous cracking” steps and mechanism are presented in this section. Multiple crack initiations were proposed using three materials’ sets intersecting an XFEM crack set. The implicit solver was used to march through the time steps of boundary/domain displacement ramp. The cracking progress through the XFEM domain is shown in Fig. 15.

The maximum principal stress was satisfied at multiple locations leading to multiple crack initiations at the fiber/matrix region, as shown in Fig. 15a. The evolution of these microcracks led to the formation of the final crack shown in Fig. 15b. The maximum principal stress criterion was reached at multiple elements where the STATUSXFEM had a value greater than zero. The STATUSXFEM continued to increase until it reached a value of unity (Fig. 15b) in one of the elements that was completely damaged based on the traction-separation law.

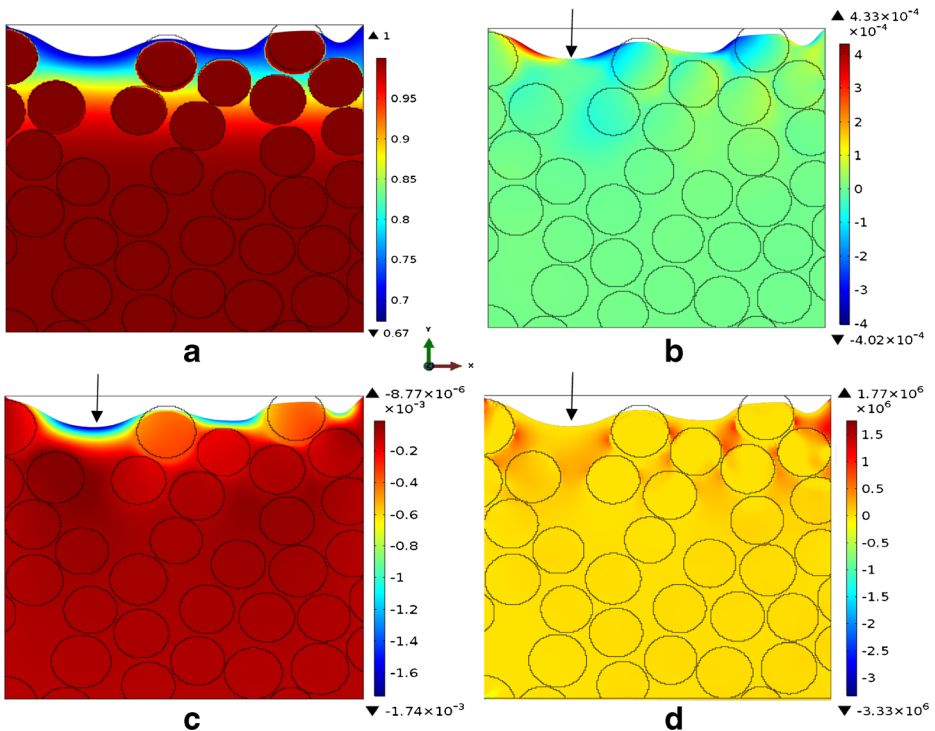


**Fig. 14** Micro-scale results **a** oxidation state, **b** and **c**  $u$  and  $v$  shrinkage displacements (unit is  $\mu\text{m}$ ), and **d** second principal stress in Pa ( $\sigma_{22}$ )

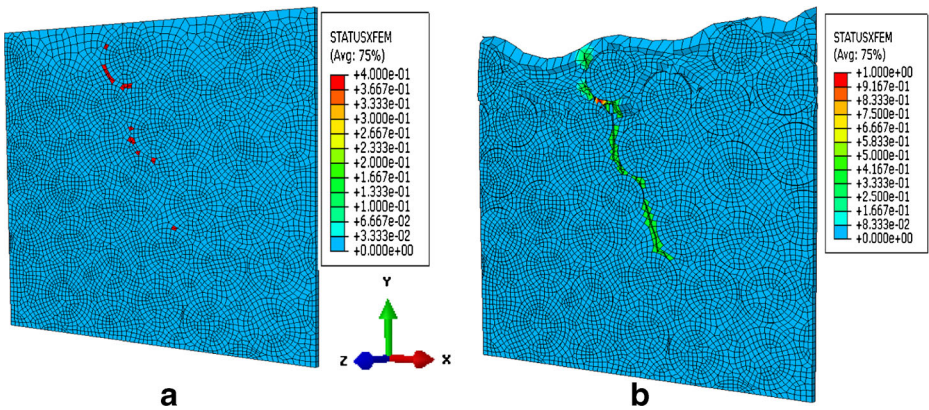


**Fig. 15** 3D Micro-scale STATUSXFEM **a** early aging hours (multiple crack initiations), **b** full crack after 500 h shrinkage displacement

However, the real crack in the SEM image was a single crack, though multiple micro-cracks initiations were also possible. The degradation of the fiber/matrix interfacial strength due to oxidation and polymer decomposition was sparse due to the spatial distribution of fibers in the matrix. Further, the average oxidized layer thickness by simulation was 7.5  $\mu\text{m}$ , which was 25% of the crack length of 30  $\mu\text{m}$ , based on the SEM image measurement. These results raise the possibility of crack initiation due to interfacial strength degradation rather than matrix oxidation. Matrix oxidation formed a stiffer oxidized layer with a higher modulus than the unoxidized matrix, which was also a possible reason behind the cracking of the inner matrix/interfaces. However, multiple crack initiations and interfacial debondings were not recognized by SEM, which requires timely monitoring with further investigation. The fracture energy and the maximum principal stress were reduced in the order of  $10^{-6}$  and  $10^{-12}$  of the values used in the literature for BMI [11]. The literature strength values were smeared for a laminate that does not reflect the local variation in the micro-scale. The remarkable reduction was attributed to the effect of polymer embrittlement induced by thermo-oxidation. Reducing the material’s properties was practical, since previous studies showed a dramatic decrease of 98% in the ductility of polypropylene tensile coupons after 150 h exposure at 90°C [25]. However, the validity of the tensile coupons

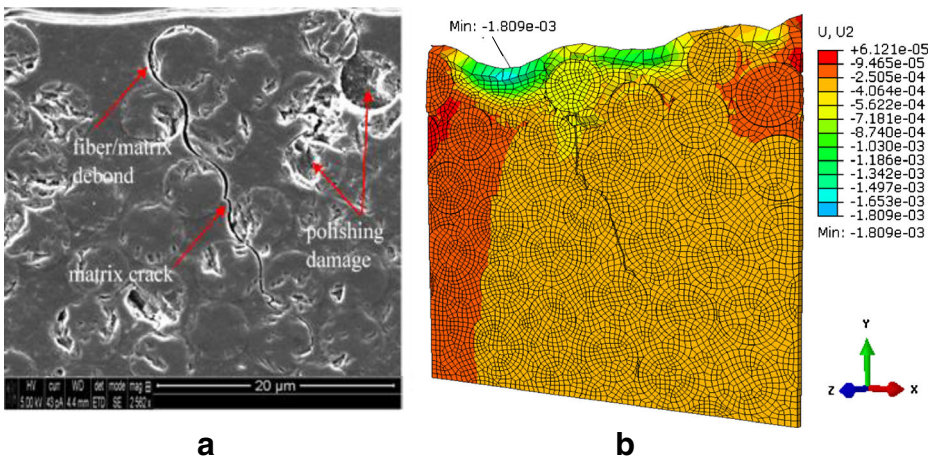


**Fig. 16** A comparison between **a** the SEM image, and **b** simulated domain cracking (displacement unit is  $\mu\text{m}$ )

was limited to the sample scale where tests are generally conducted. Precise measurements of the local properties for a composite is challenging and requires efficient simulation to investigate the degradation and damage reaching better assessments of the composite behavior at lower scales.

The crack length, meander, and opening are well simulated using the multi-scale approach of the current work, as shown in Fig. 16. However, the crack length did not exactly match. The shrinkage of the real SEM image was not directly comparable to the simulation shrinkage due to the difference in scale. The shrinkage displacement of  $1.809 \times 10^{-3} \mu\text{m}$  happened at 500 h of aging, leading to the crack formation. It should be noted that the results were based on assumed fracture energy and maximum principal stress, the determination of which is challenging. The real scenario of damage events was assumed and simulated, but it needs to be generalized for multiple cases where the issue of the locality is challenging.

## 7 Conclusions

High temperature polymer matrix composites are used under extreme environments where thermo-oxidation is the dominating degradation mechanism. Better understanding of the degradation and the associated shrinkage and cracking damage is required to predict the mechanical behavior and service life. In the current work, a multiscale approach was proposed to simulate the shrinkage deformation and micro-scale cracking damage. The effects of the global thermo-oxidation on the local boundary conditions were considered by running macro- and meso-scale simulations and extracting the induced 3D displacements ( $u$ ,  $v$ , and  $w$ ). These displacement boundary conditions were then applied to the respective micro-scale simulations utilizing an OOF-generated mesh and geometry. The oxidative macro-shrinkage strain was assumed linearly dependent on the oxidation state variable and attains its maximum value  $\varepsilon_s^{ox} = 2.5 \times 10^{-5}$  when the matrix is completely oxidized. The maximum shrinkage strain was assumed as a material property determined by measuring the volumetric shrinkage of a unidirectional coupons aged under 200°C. However, the local value of the maximum shrinkage strain was  $\varepsilon_s^{ox}(local) = 3.25 \times 10^{-4}$  and had the local crack matched to the SEM image measurements. This suggested a distribution of the form  $\varepsilon_s^{ox}(local) = f(x, y, z)$  similar to all material properties. Since testing is not practical at the local scale, powerful simulation schemes are necessary under reasonable assumptions especially, the boundary conditions. The microcracking was validated using a 3D static simulation to the OOF-generated/replicated mesh and geometrical domain. Despite, the transient nature, cooling/heating cycles during aging, and the evolution of the thermal transport and thermal expansion coefficient being not considered, the cracking simulation results were good. The reduction in the fracture energy and the maximum principal stress was in the order of  $10^{-6}$  and  $10^{-12}$  of the smeared values used in the literature for BMI. This was attributed to the oxidation-induced embrittlement and the effects of local stress concentration at the fiber/matrix interface. The interfacial strength was also considered to be in the same level of reduction for the cohesive surface contacts. Not only was the crack length closely simulated, but also the crack meander and opening. However, the procedure was validated for a real crack; a plethora of future validation cases are required to generalize the approach.

### Compliance with Ethical Standards

**Conflict of Interest** The authors declare that they have no conflict of interest.

## References

1. Langer, S., Fuller, E.R., Carter, W.C.: OOF: an image-based finite-element analysis of material microstructures. *Comput. Sci. Eng.* **3**, 15–23 (2001)
2. Reid, A.C.E., Langer, S.A., Lua, R.C., Coffman, V.R., Haan, S.-I., Garcia, R.E.: Image-based finite element mesh construction for material microstructures. *Comput. Mater. Sci.* **43**, 989–999 (2008)
3. Reid, A.C.E., Lua, R.C., Garcia, R.E., Coffman, V.R., Langer, S.A.: Modeling microstructures with OOF2. *Int. J. Mater. Prod. Technol.* **35**, 361–373 (2009)
4. Coffman, V.R., Reid, A.C.E., Langer, S.A., Dogan, G.: OOF3D: an image-based finite element solver for materials science. *Math. Comput. Simul.* **82**, 2951–2961 (2012)
5. Goel, A., Chawla, K.K., Vaidya, U.K., Chawla, N., Koopman, M.: Two dimensional microstructure based modelling of Young's modulus of long fibre thermoplastic composite. *Mater. Sci. Technol.* **24**, 864–869 (2008)
6. Dong, Y., Bhattacharyya, D.: Two dimensional microstructure based modelling of Young's modulus of long fibre thermoplastic composite. *Mech. Adv. Mater. Struct.* **17**, 534–541 (2010)
7. Dong, Y., Bhattacharyya, D.: Mapping the real micro/nanostructures for the prediction of elastic moduli of polypropylene/clay nanocomposites. *Polymer* **51**, 816–824 (2010)
8. Decelle, J., Huet, N., Bellenger, V.: Oxidation induced shrinkage for thermally aged epoxy networks. *Polym. Degrad. Stab.* **81**, 239–248 (2003)
9. Pochiraju, K.V., Tandon, G.P., Schoepner, G.A.: Evolution of stress and deformations in high-temperature polymer matrix composites during Thermo-oxidative aging. *Mech. Time-Depend. Mater.* **12**, 45–68 (2008)
10. Gigliotti, M., Olivier, L., Vu, D.Q., Grandidier, J., Lafarie-Frenot, M.C.: Local shrinkage and stress induced by Thermo-oxidation in composite materials at high temperatures. *J. Mech. Phys. Solids.* **59**, 696–712 (2011)
11. An, N., Pochiraju, K.: Modeling Damage Growth in Oxidized High-Temperature Polymeric Composites. *J. Miner. Met. Mater. Soc. (TMS)* **65**, 246–255 (2013)
12. Liang, J., Pochiraju, K.: Oxidation-induced damage evolution in a unidirectional polymer matrix composite. *J. Compos. Mater.* **49**, 1393–1406 (2015)
13. Daghia, F., Zhang, F., Cluzel, C., Ladevèze, P.: Thermo-Mechano-oxidative behavior at the Ply's scale: the effect of oxidation on transverse cracking in carbon–epoxy composites. *Compos. Struct.* **134**, 602–612 (2015)
14. Schoepner, G.A., Tandon, G.P., Ripberger, E.R.: Anisotropic oxidation and weight loss in PMR-15 composites. *Compos. Part A* **38**, 890–904 (2007)
15. Upadhyaya, P., Roy, S., Haque, M.H., Lu, H.: Influence of Nano-clay compounding on Thermo-oxidative stability and mechanical properties of a thermoset polymer system. *Compos. Sci. Technol.* **84**, 8–14 (2013)
16. Haque, M.H., Upadhyaya, P., Roy, S., Ware, T., Voit, W., Lu, H.: The changes in flexural properties and microstructures of carbon fiber Bismaleimide composite after exposure to a high temperature. *Compos. Struct.* **108**, 57–64 (2014)
17. Tuttle, M.E.: Structural analysis of polymeric composite materials. Second Edition, 2013. CRC Press, Taylor & Francis Group, Boca Raton, FL (2003)
18. Hussein, R.M., Anandan, S., Chandrashekhara, K.: Flexural behavior of cross-ply thermally aged Bismaleimide composites CAMX conference Proceedings, Anaheim, 26–29 September 2016
19. W-F, W., Cheng, H.-C., Kang, C.-K.: Random field formulation of composite laminates. *Compos. Struct.* **49**, 87–93 (2000)
20. Barber, A., Kaplanashiri, I., Cohen, S., et al.: Stochastic strength of nanotubes: an appraisal of available data. *Compos. Sci. Technol.* **65**, 2380–2384 (2005)
21. Asadpoure, A., Mohammadi, S., Vafaia, A.: Modeling crack in orthotropic media using a coupled finite element and partition of Unity methods. *Finite Elem. Anal. Des.* **42**, 1165–1175 (2006)
22. Huynh, D.B.P., Belytschko, T.: The extended finite element method for fracture in composite materials. *Int. J. Numer. Methods Eng.* **77**, 214–239 (2009)
23. Ebrahimi, S.H., Mohammadi, S., Asadpoure, A.: An extended finite element (XFEM) approach for crack analysis in composite media. *Int. J. Civ. Eng.* **6**, 198–207 (2008)
24. Hussein, R.M., Anadan, S., Chandrashekhara, K.: Anisotropic oxidation prediction using optimized weight loss models of Bismaleimide composites. *J. Mater. Sci.* **51**, 7236–7253 (2016)
25. Fayolle, B., Audouin, L., Verdu, J.: Oxidation induced embrittlement in polypropylene –a tensile testing study. *Polym. Degrad. Stab.* **70**, 333–340 (2000)